

# Feedback under the microscope: thermodynamic structure and AGN driven shocks in M 87

E. T. Million<sup>1</sup>, N. Werner<sup>1</sup>, A. Simionescu<sup>1</sup>, S. W. Allen<sup>1</sup>,  
P. E. J. Nulsen<sup>2</sup>, A. C. Fabian<sup>3</sup>, H. Böhringer<sup>4</sup>, and J. S. Sanders<sup>3</sup>

<sup>1</sup>*Kavli Institute for Particle Astrophysics and Cosmology, Stanford University, 382 Via Pueblo Mall, Stanford, CA 94305-4060, USA;*

*SLAC National Accelerator Laboratory, 2575 Sand Hill Road, Menlo Park, CA 94025, USA*

<sup>2</sup>*Harvard-Smithsonian Center for Astrophysics, 60 Garden St., Cambridge, MA, 02138, USA*

<sup>3</sup>*Institute of Astronomy, Madingley Road, Cambridge CB3 0HA*

<sup>4</sup>*Max-Planck-Institut für extraterrestrische Physik, Giessenbachstr, 85748 Garching, Germany*

30 June 2010

## ABSTRACT

We present the second in a series of papers discussing the thermodynamic properties of M87 and the central regions of the Virgo Cluster in unprecedented detail. Using a deep *Chandra* exposure (574 ks), we present high-resolution thermodynamic maps created from the spectra of  $\sim 16,000$  independent regions, each with  $\sim 1,000$  net counts. The excellent spatial resolution of the thermodynamic maps reveals the dramatic and complex temperature, pressure, entropy and metallicity structure of the system. The ‘X-ray arms’, driven outward from M87 by the central AGN, are prominent in the brightness, temperature, and entropy maps. Excluding the ‘X-ray arms’, the diffuse cluster gas at a given radius is strikingly isothermal. This suggests either that the ambient cluster gas, beyond the arms, remains relatively undisturbed by AGN uplift, or that conduction in the intracluster medium (ICM) is efficient along azimuthal directions, as expected under action of the heat-flux driven buoyancy instability (HBI). We confirm the presence of a thick ( $\sim 40$  arcsec or  $\sim 3$  kpc) ring of high pressure gas at a radius of  $\sim 180$  arcsec ( $\sim 14$  kpc) from the central AGN. We verify that this feature is associated with a classical shock front, with an average Mach number  $M = 1.25$ . Another, younger shock-like feature is observed at a radius of  $\sim 40$  arcsec ( $\sim 3$  kpc) surrounding the central AGN, with an estimated Mach number  $M \gtrsim 1.2$ . As shown previously, if repeated shocks occur every  $\sim 10$  Myrs, as suggested by these observations, then AGN driven weak shocks could produce enough energy to offset radiative cooling of the ICM. A high significance enhancement of Fe abundance is observed at radii  $350 - 400$  arcsec ( $27 - 31$  kpc). This ridge is likely formed in the wake of the rising bubbles filled with radio-emitting plasma that drag cool, metal-rich gas out of the central galaxy. We estimate that at least  $\sim 1.0 \times 10^6$  solar masses of Fe has been lifted and deposited at a radius of  $350 - 400$  arcsec; approximately the same mass of Fe is measured in the X-ray bright arms, suggesting that a single generation of buoyant radio bubbles may be responsible for the observed Fe excess at  $350 - 400$  arcsec.

**Key words:** X-rays: galaxies: clusters – galaxies: individual: M 87 – galaxies: intergalactic medium – cooling flows

## 1 INTRODUCTION

The Virgo Cluster is the second brightest, extragalactic, extended X-ray source in the  $0.1 - 2.4$  keV ROSAT band, and the closest galaxy cluster (16.1 Mpc; Tonry *et al.* 2001). The central galaxy of the Virgo Cluster, M87, hosts an active galactic nucleus (AGN) that exhibits compelling evidence for complex interactions with the surrounding cluster gas

(*e.g.* Böhringer *et al.* 1995; Young *et al.* 2002; Forman *et al.* 2005, 2007). M87 is, therefore, an *excellent* object with which to study AGN driven processes (*i.e.* AGN feedback) that affect the centers of galaxies and galaxy clusters.

The relatively cool, dense gas at the centers of many galaxy clusters emits copiously at X-ray wavelengths. In the absence of a significant heat source, this gas would be ex-

pected to cool quickly and promote significant star formation, at rates an order of magnitude larger than observed (see Peterson & Fabian 2006 for a review). The energy required to offset this cooling is widely believed to come predominantly from the central AGN, though the exact process or processes by which this occurs remains unclear (see *e.g.* McNamara & Nulsen 2007). AGN inflate bubbles of relativistic radio plasma, which displace the X-ray emitting gas, forming clear cavities. This process is expected to provide a significant source of heating and turbulence (Churazov *et al.* 2001; see also *e.g.* Brüggen & Kaiser 2002; Kaiser 2003; Brüggen 2003; De Young 2003; Ruszkowski *et al.* 2004a,b; Heinz & Churazov 2005). Sound waves and internal waves generated by cavity inflation also provide a mechanism to heat the intra-cluster medium (ICM). These waves have been observed in both the Perseus and Centaurus clusters (*e.g.* Fabian *et al.* 2003; Fabian *et al.* 2006; Sanders & Fabian 2007; Sanders & Fabian 2008). AGN induced shock activity is a further promising avenue to heat the ICM. Clear indications of AGN-induced shocks are seen in several nearby galaxies and clusters, the best examples being Hydra A, Virgo, and Perseus clusters (*e.g.* Nulsen *et al.* 2005a; Simionescu *et al.* 2009; Forman *et al.* 2005, 2007; Fabian *et al.* 2003, 2006). AGN induced shocks in clusters are typically weak; Hercules A hosts the strongest observed AGN driven shock in a cluster with a Mach number  $M \sim 1.65$  (Nulsen *et al.* 2005b). These outbursts can also be very energetic; MS 0735+7421 boasts the highest observed energy with  $\sim 6 \times 10^{61}$  ergs associated with its shock (Gitti *et al.* 2007). In galaxies and galaxy groups, these shocks can be much stronger with Mach numbers as high as  $M \sim 8$  as observed in Centaurus A (Croston *et al.* 2009; Kraft *et al.* 2003). In M 87, Forman *et al.* (2005) identified shock fronts associated with an AGN outburst  $\sim 1 - 2 \times 10^7$  years ago. They argued that shocks may be the most significant mechanism of heating the cool ICM near the core by the AGN. Forman *et al.* (2007) also measure temperature and density jumps that are consistent with a weak shock with Mach number  $M \sim 1.2$ . However, important uncertainties remain. For example, significant temperature jumps are not seen across all putative shock fronts (*e.g.* Graham *et al.* 2008). Additionally, the observed pressure features are sometimes several kpc thick (Fabian *et al.* 2006), complicating our understanding of how these processes work.

In M 87, two X-ray bright ‘arms’, discovered by Feigelson *et al.* (1987) using the *Einstein Observatory*, are the most striking features driven by AGN activity. These arms extend to the southwest and east of the galactic center, are composed of cool gas, and are spatially coincident with extended radio emission (Böhringer *et al.* 1995; Belsole *et al.* 2001; Molendi 2002). Böhringer *et al.* (1995; see also Churazov *et al.* 2001) propose that these structures are the result of gas uplift in the wakes of bubbles of radio plasma buoyantly rising in the hot ICM. However, the details of this process and the role of magnetic fields are largely not understood. Subsequent *Chandra* and *XMM-Newton* observations of M 87 have revealed many additional complexities in the system (*e.g.* Belsole *et al.* 2001; Matsushita *et al.* 2002; Molendi 2002; Böhringer *et al.* 2002; Sakelliou *et al.* 2002; Young *et al.* 2002; Forman *et al.* 2005, 2007; Simionescu *et al.* 2007, 2008; Werner *et al.* 2006).

Here, we present the second in a series of papers study-

**Table 1.** Summary of the *Chandra* observations of M 87 used in this study. Columns list the observation ID, detector, observation mode, exposure after cleaning and observation date.

Obs. ID	Obs. Date	Detector	Mode	Exp. (ks)
2707	Jul. 6 2002	ACIS-S	FAINT	82.9
3717	Jul. 5 2002	ACIS-S	FAINT	11.1
5826	Mar. 3 2005	ACIS-I	VFAINT	126.8
5827	May 5 2005	ACIS-I	VFAINT	156.2
5828	Nov. 17 2005	ACIS-I	VFAINT	33.0
6186	Jan. 31 2005	ACIS-I	VFAINT	51.5
7210	Nov. 16 2005	ACIS-I	VFAINT	30.7
7211	Nov. 16 2005	ACIS-I	VFAINT	16.6
7212	Nov. 14 2005	ACIS-I	VFAINT	65.2

ing in unprecedented detail the thermodynamic properties of M 87. Using an ultra-deep (574 ks) observation, we utilize fully the excellent spatial resolution of the *Chandra X-ray Observatory*. This paper focuses on the overall thermodynamic structure and Fe distribution of the galaxy and surrounding cluster, and on the properties of the strongest shock features. Other papers will study the detailed physics of the X-ray bright arms and inner post-shock regions (Werner *et al.* 2010; hereafter Paper I) and the history of chemical enrichment (Million *et al.* 2010, in prep; Paper III).

The structure of this paper is as follows. Section 2 describes the data reduction, basic imaging analysis, and spatially resolved spectroscopy. Section 3 presents detailed thermodynamic maps for the cluster. Section 4 presents results on the radial properties of the ambient ICM to the north and south of the AGN; this excludes the X-ray bright arms, which introduce strong multi-temperature structure into the profiles. We place important new constraints on the isothermality of the ambient cluster gas. Section 5 discusses the results, focusing on the shock features at radius  $r \sim 180$  arcsec, the isothermality of the ambient cluster gas, and a high significance metallicity bump at  $r \sim 5 - 6$  arcmin. Section 6 summarizes our conclusions.

Throughout this paper, we assume that the cluster lies at a distance of 16.1 Mpc, for which the linear scale is 0.078 kpc per arcsec.

## 2 X-RAY OBSERVATIONS AND ANALYSIS

### 2.1 Data Reduction

Our work builds upon previous analyses of the same datasets studied here (see Young *et al.* 2002; Forman *et al.* 2005, 2007). The *Chandra* observations were carried out using the Advanced CCD Imaging Spectrometer (ACIS) between July 2002 and November 2005. The standard level-1 event lists produced by the *Chandra* pipeline processing were reprocessed using the *CIAO* (version 3.5.0) software package, including the appropriate gain maps and updated calibration products. Bad pixels were removed and standard grade selections applied. Where possible, the extra information available in VFAINT mode was used to improve the rejection of cosmic ray events. The data were cleaned to remove periods of anomalously high background using the standard energy ranges recommended by the *Chandra* X-ray Center. The net

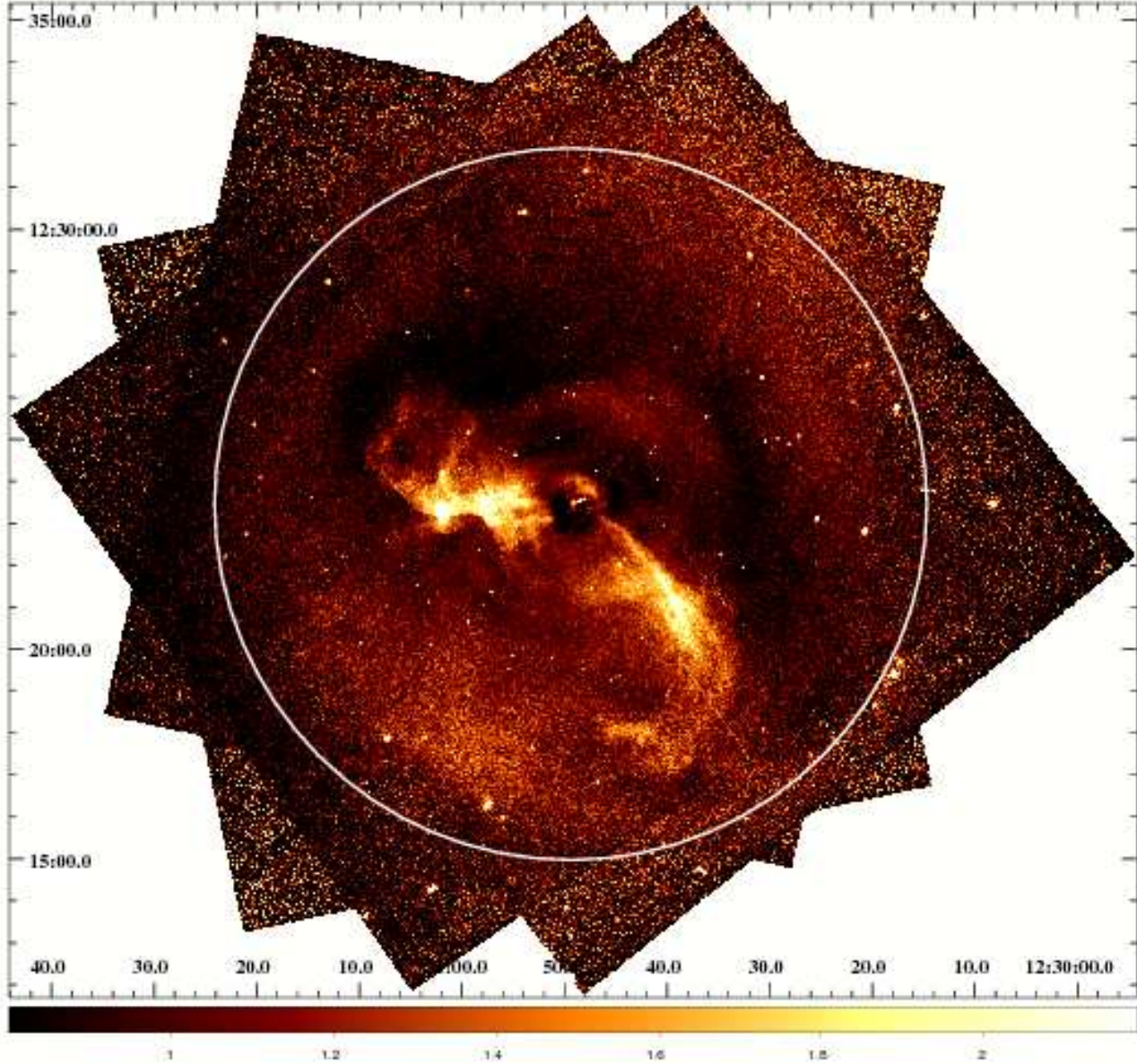


**Figure 1.** Exposure corrected, flat-fielded, surface brightness image of the central regions of the Virgo Cluster divided by the best-fit, radially symmetric double- $\beta$  model in the 0.6 – 2.0 keV energy band and smoothed with a 2 arcsec Gaussian. Unity represents locations where the data is equal to the model. This image uses only the ACIS-I data taken in 2005. The white circle represents the outer extent of the thermodynamic maps presented in Figs. 2-5 (radius 8.5 arcmin or  $\sim 40$  kpc).

exposure times after cleaning are summarized in Table 1 and total 574 ks. Separate photon-weighted response matrices and effective area files were constructed for each region analyzed.

## 2.2 Imaging analysis

Background subtracted images on a  $0.984 \times 0.984$  arcsec<sup>2</sup> pixel scale were created for each pointing in many narrow energy bands (spanning 0.6 – 7.0 keV). These were flat-fielded with respect to the median energy for each image. Background images were created from the blank-sky fields avail-

able from the *Chandra* X-ray Center. The blank-sky fields were processed in an identical manner to the science observations and were reprojected onto the same coordinates using the aspect solution files. The background images were normalized by the ratio of the observed and blank-sky count rates in the 9.5 – 12 keV band. The images were summed to form a series of combined background subtracted, exposure corrected images. Fig. 1 shows the X-ray image in the



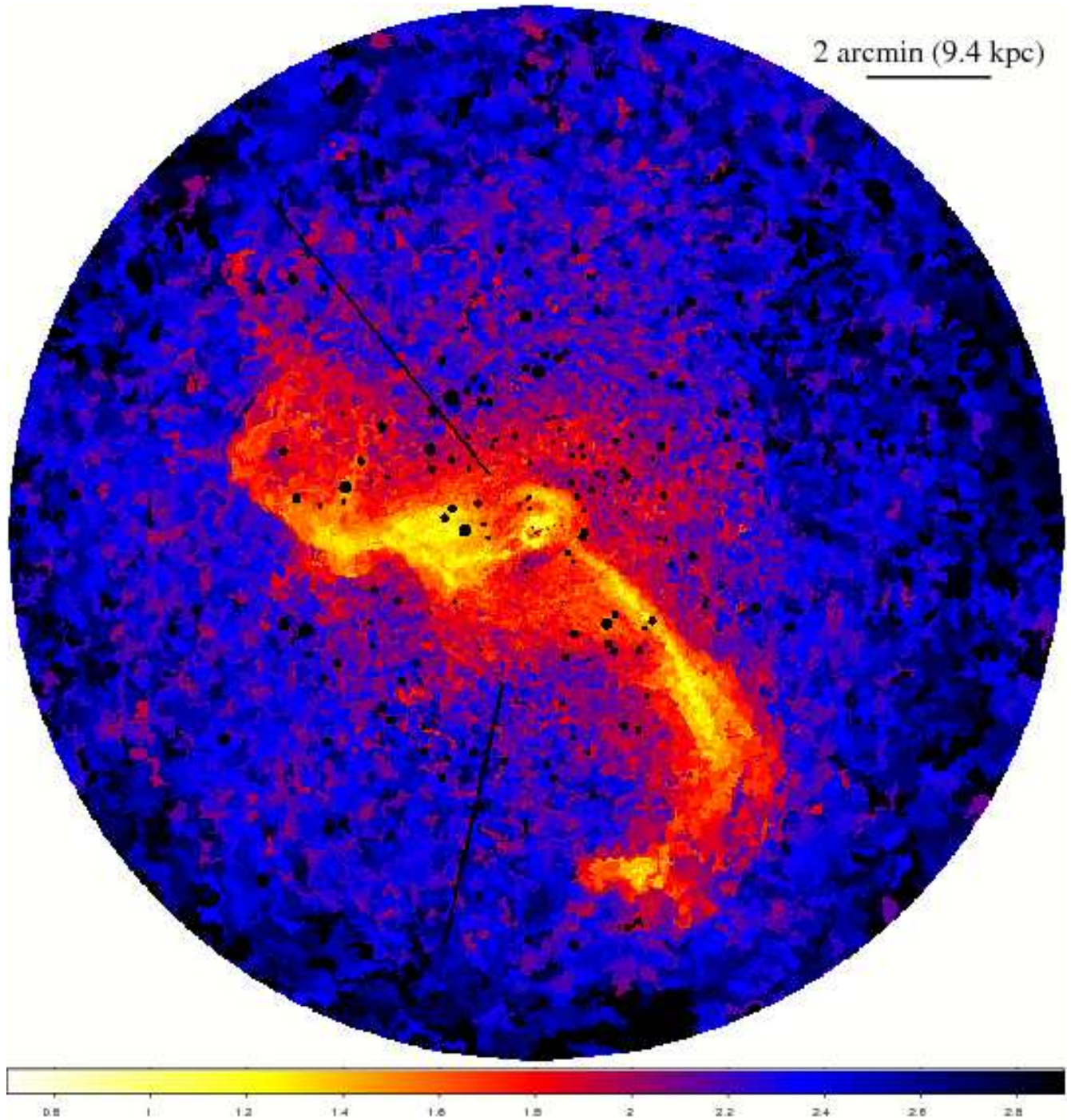


**Figure 2.** Temperature map of the central regions of the Virgo Cluster (in units of keV) for the 8.5 arcmin ( $\sim 40$  kpc) radius region indicated by the white circle in Fig. 1. Regions have  $\sim 1,000$  net counts, leading to  $1\sigma$  fractional uncertainties in the plotted quantities of  $\sim 10$  per cent. Point sources, and readout errors have been excluded in this analysis and appear as black holes in the maps.

0.6 – 2.0 keV band divided by the best-fit, double- $\beta$  model<sup>1</sup> and smoothed with a 2 arcsec filtered Gaussian. This image spans the entire region covered by ACIS-I observations

<sup>1</sup> In detail, this is the sum of two  $\beta$  models of the form  $S_0 \left[ 1 + \left( \frac{r}{r_c} \right)^2 \right]^{-\alpha}$ , where  $S_0$  is the amplitude of the X-ray surface brightness,  $r_c$  is the core radius, and  $\alpha$  is the power-law index.

taken in 2005. The white circle ( $r \sim 8.5$  arcmin) denotes the outer extent of the data used for the spectral analysis reported here.

The cool X-ray arms are readily apparent in the image. An extensive imaging analysis of these data is presented by Forman *et al.* (2007).

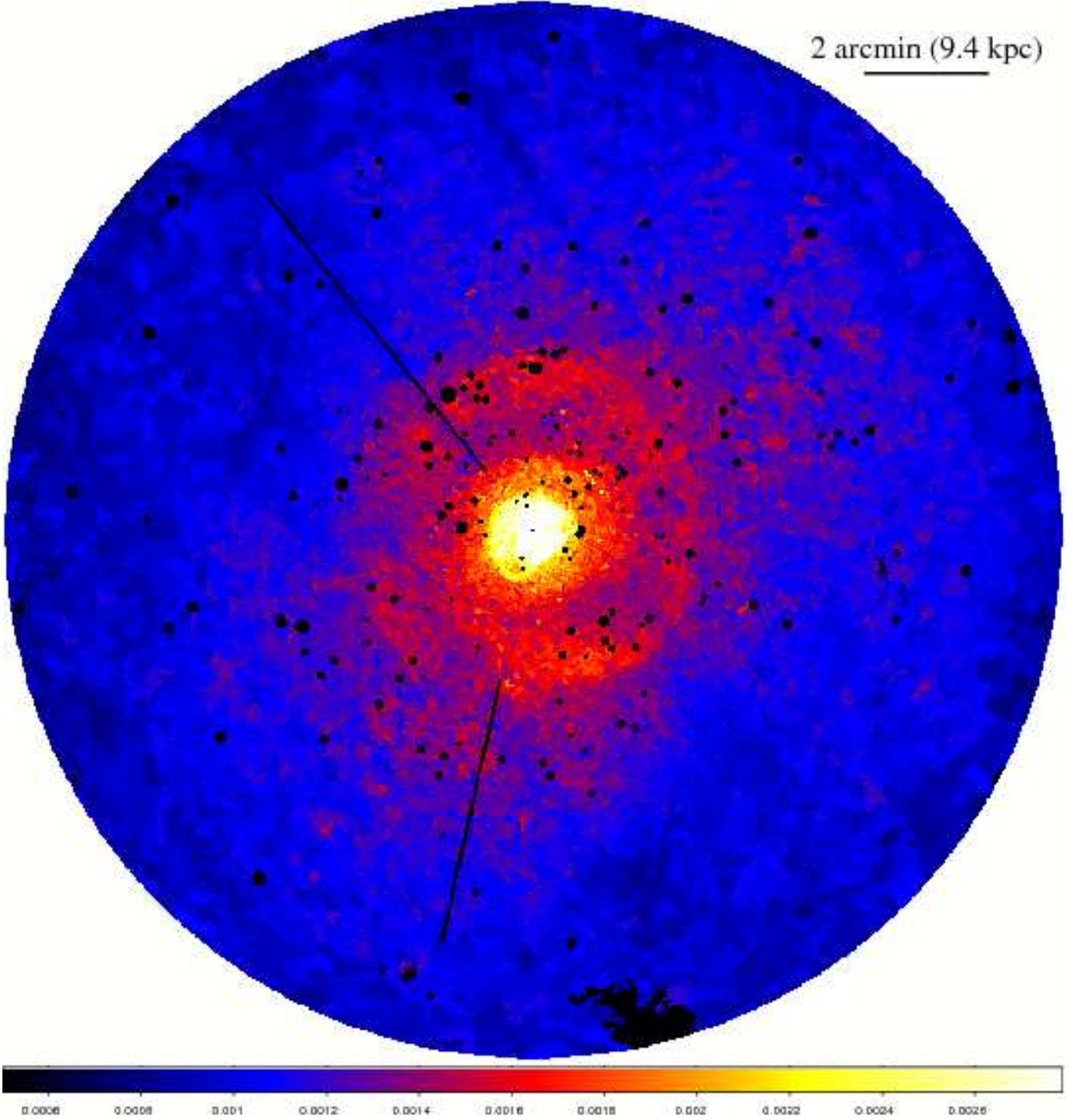


**Figure 3.** Pressure map in units of  $\text{keV cm}^{-3} \times \left(\frac{l}{2 \text{ Mpc}}\right)^{-1/2}$ . The number density was calculated from the normalization of the spectra;  $n_e = \sqrt{\frac{CK}{Al}}$ , where  $K$  is the MEKAL normalization,  $A$  the projected area, and  $l$  the line-of-sight depth.  $C = 10^{14} \times 4\pi D_L^2/1.2$  and depends only on the distance to the source. We assume that the line-of-sight depth is  $l = 2 \text{ Mpc}$  over the field of view. Other details as for Fig. 2.

## 2.3 Spatially-resolved spectroscopy

### 2.3.1 Contour binning

The individual regions for spectral fitting were determined using the contour binning method of Sanders (2006), which groups neighboring pixels of similar surface brightness until

a desired signal-to-noise threshold is met. For data of the quality discussed here, regions outside the X-ray bright arms are small enough that the X-ray emission from each can be approximated usefully by a single temperature plasma model. Regions inside the X-ray bright arms show strong evidence for multi-phase gas (see Paper I). In this paper,



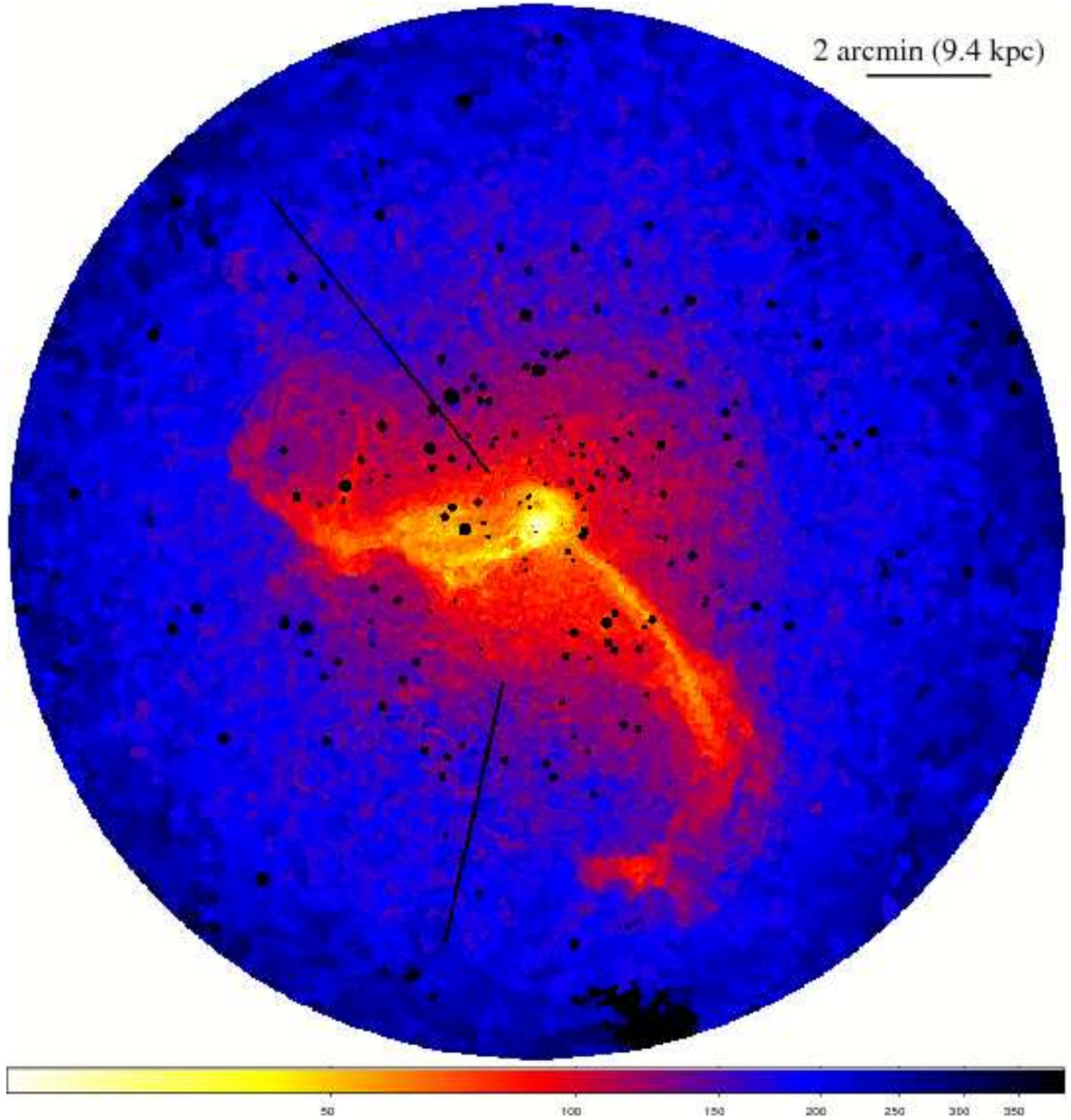


**Figure 4.** Entropy map of M87 in units of  $\text{keV cm}^2 \times \left(\frac{l}{2\text{Mpc}}\right)^{1/3}$ . Other details as for Fig. 3.

however, as a first approximation, we model all regions as a single temperature plasma, recognizing that this will bias the results for the X-ray bright arms.

We constrain each region to have  $\sim 10^3$  net counts, giving  $\sim 16,000$  total regions for a total of  $\sim 16,000,000$  net counts. This number of counts is sufficient to determine the temperature of the cluster gas to  $\lesssim 10$  per cent and the metallicity to  $\sim 20$  per cent in each of the  $\sim 16,000$  independent spatial bins. The density of the cluster gas is always determined to higher precision. We have imposed a lower

limit on the region size of one  $\text{arcsec}^2$ , to mitigate the effects of *Chandra's* point spread function. Regions vary in size from one to approximately  $5,000 \text{ arcsec}^2$  in the outer regions. Because the statistical uncertainty of the best-fit metallicity is  $\sim 20$  per cent for regions with 1,000 counts, we have also performed a second analysis with regions containing at least 2,500 net counts each. This latter analysis produces statistical uncertainties of 3 – 5 per cent on the temperature and  $\sim 15$  per cent on the metallicity.

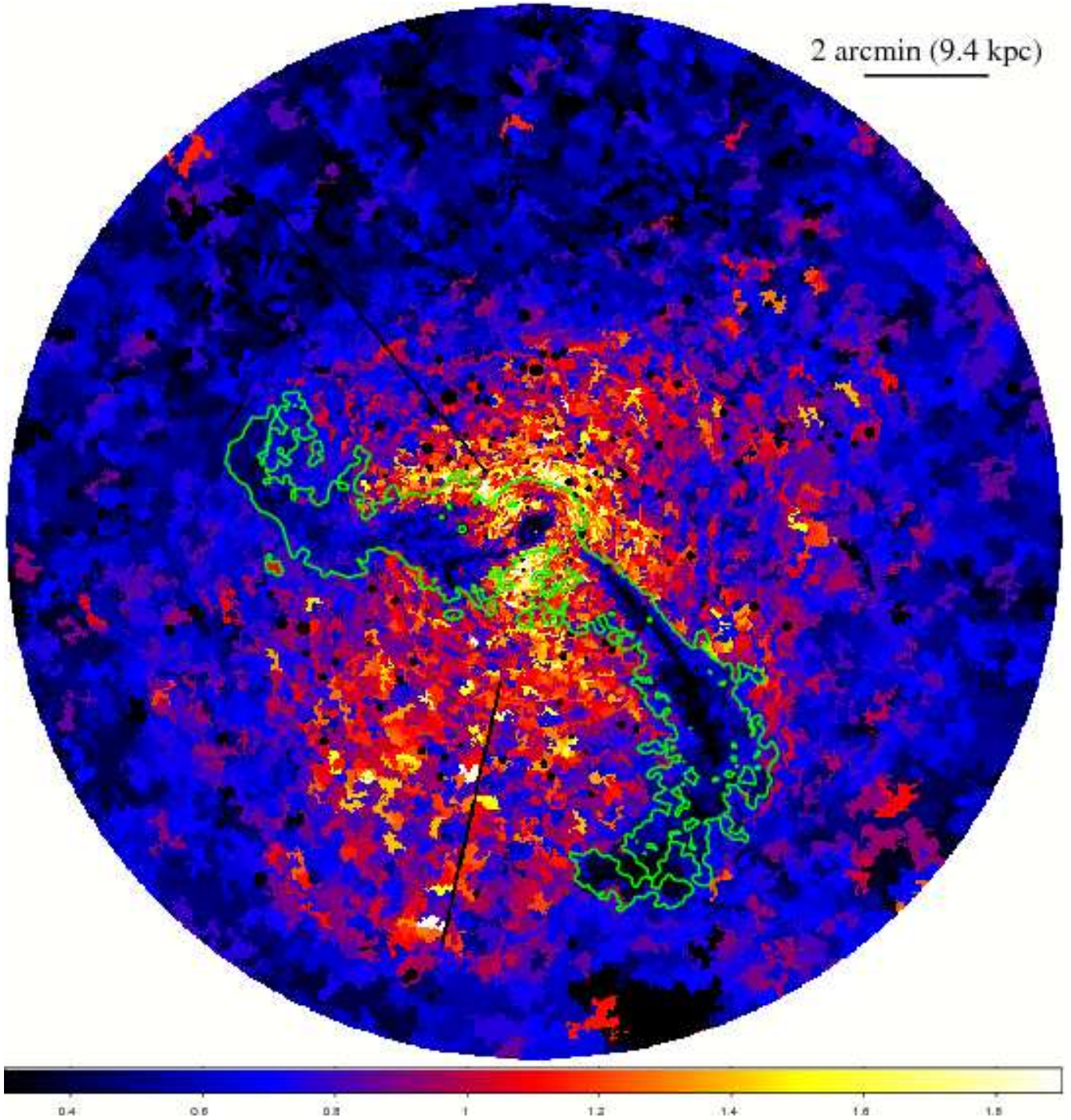


**Figure 5.** Metallicity map in solar units. Abundances are with respect to the proto-solar values of Lodders *et al.* (2003). Regions contain at least 2,500 net counts each. This results in statistical uncertainties of  $\sim 15$  per cent per region. Regions inside the green contours contain significant 1 keV emission (see Fig. 2; Paper I) and are modelled improperly by a single temperature plasma. As a result, the metallicity in these regions is significantly underestimated (*e.g.* Buote *et al.* 2000; Simionescu *et al.* 2008; Werner *et al.* 2008). Other details as for Fig. 2.

### 2.3.2 Annular binning

To better study the properties of the ambient cluster gas, we have also performed a radial analysis in which we exclude the X-ray bright arms. This simplifies greatly the interpretation of the results. For this analysis, we use annuli that vary in width from 10 to 30 arcsec, with  $\sim 250,000$  net counts in

each for a total of 36 annuli. Each annulus is fitted with a single temperature MEKAL or APEC spectral model (Section 2.3.3) with Galactic absorption. We have analyzed the northern (position angles<sup>2</sup> -135 to 86 degrees) and southern

<sup>2</sup> All position angles are measured counter-clockwise from north.



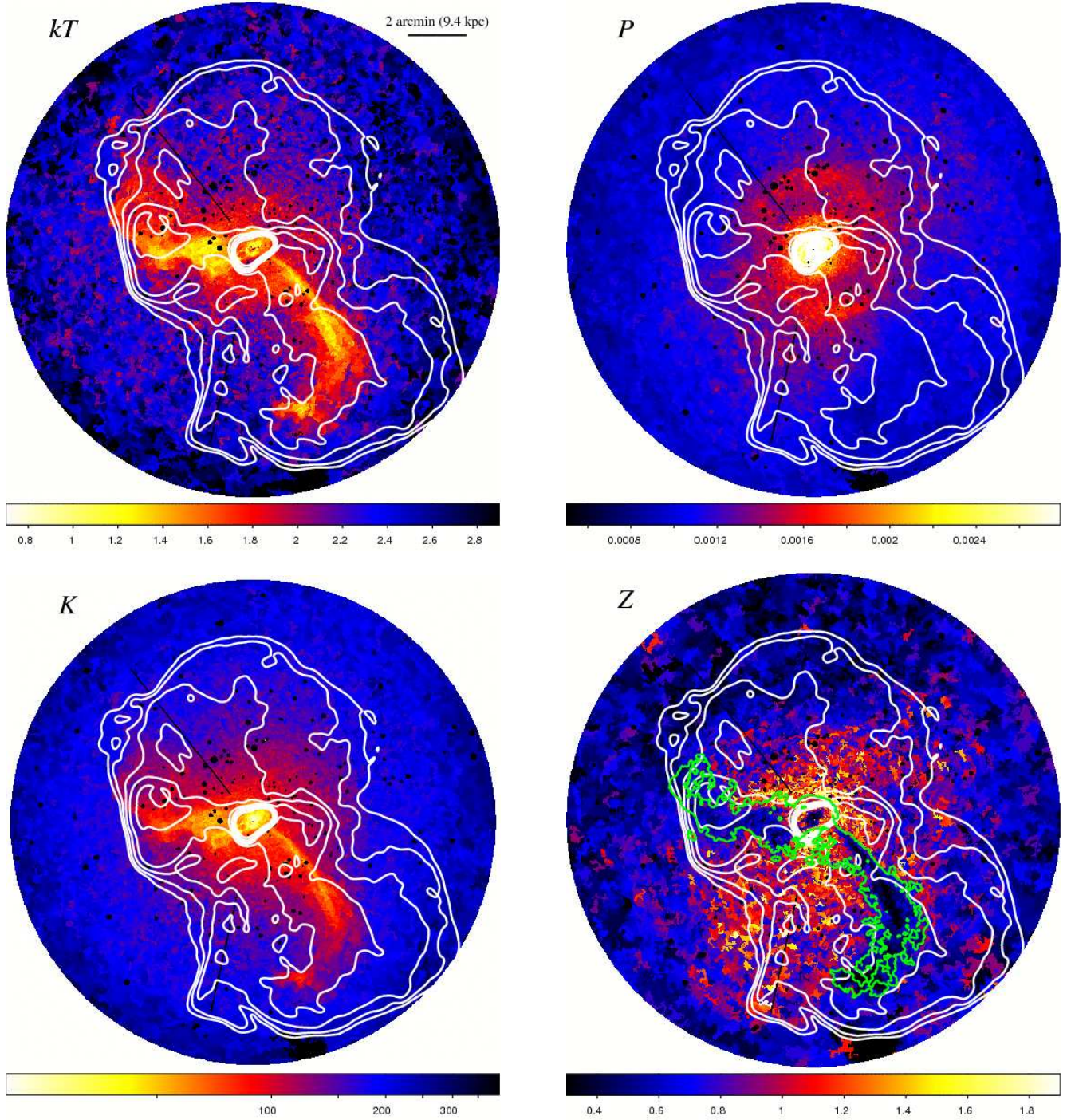


**Figure 6.** Temperature ( $kT$ ), pressure ( $P$ ), entropy ( $K$ ), and metallicity ( $Z$ ) maps with the 90 cm radio contours from Owen *et al.* (2000) overplotted. Other details as for Fig. 2–5.

(position angles 86 to 225 degrees) profiles both separately and together, always excluding the arms.

### 2.3.3 Plasma models

The spectra have been analyzed using XSPEC (version 12.5; Arnaud 1996). We use the MEKAL and APEC plasma emission codes (Kaastra & Mewe 1993; Smith *et al.* 2001), and the photoelectric absorption models of Balucinska-Church &

McCammon (1992). All spectral fits were carried out in the 0.6 – 7.0 keV energy band. The extended C-statistic available in XSPEC, which allows for background subtraction, was used for all fitting.

The spectral model, applied to each spatial region, consists of an optically-thin, thermal plasma model, at the redshift of the cluster. We fix the Galactic absorption to  $1.93 \times 10^{20}$  atom  $\text{cm}^{-2}$  (determined from the *Leiden/Argentine/Bonn* radio HI survey; Kalberla *et al.*



2005). The temperature, metallicity, and the normalization are free parameters for every region (in detail, the normalizations for each observation of each region are independently free). In determining the metallicity from the 2-dimensional spectral maps, all abundances are assumed to vary in a fixed ratio with respect to solar. In our higher signal-to-noise analysis of annular spectra, (see Section 4), we have allowed the abundances of O, Ne, Mg, Si, S, Ar, Ca, Fe, and Ni to be separate, free parameters. Results on the abundances of individual elements will be presented in a subsequent paper (Paper III). Abundances are given with respect to the ‘proto-solar’ values of Lodders (2003).

### 2.3.4 Background modelling

Background spectra for the appropriate detector regions were extracted from the blank-sky fields available from the *Chandra* X-ray Center. The blank-sky fields were processed in an identical manner to the science observation and were reprojected onto the same coordinates using the aspect solution files. Background regions were chosen to match the extraction regions for the science observations. The backgrounds were normalized by the ratio of the observed and blank-sky count rates in the 9.5 – 12 keV band (the statistical uncertainty in the observed 9.5 – 12 keV flux is less than 5 per cent in all cases). Due to the very small effective area of the *Chandra* telescope at hard X-ray energies, there is no significant cluster emission in the 9.5 – 12 keV band. Due to the high X-ray brightness of the target, uncertainties in the background modelling have little impact on the determination of thermodynamic quantities presented here.

## 3 THERMODYNAMIC MAPS

### 3.1 Large-scale thermodynamic properties

Figs. 2–5 show the projected temperature, pressure, entropy, and metallicity maps determined from our analysis. Fig. 6 shows the same figures in mosaic form with the 90 cm (333 MHz) radio contours from Owen *et al.* (2000) overlaid. Point sources and read-out errors have been masked and ignored. These results confirm spectrally, for the first time, many of the features identified by Forman *et al.* (2005, 2007) from an imaging analysis of the same data-set.

The temperature map shown in Fig. 2 dramatically reveals the complex temperature structure of the system. The X-ray bright arms stand out as relatively cool structures (Belsole *et al.* 2001; Young *et al.* 2002; Matsushita *et al.* 2002; Molendi 2002; Forman *et al.* 2005; Simionescu *et al.* 2007, 2008). They are spatially correlated with enhanced 90 cm radio emission (Fig. 6a; contours are overlaid in white; from Owen *et al.* 2000). However, within  $\sim 3$  arcmin (the radius of the shock front described in Section 5.2.1), the southwestern arm does not coincide precisely with the radio emission (see Fig. 6a; see also Forman *et al.* 2005, 2007).

Outside of the cool arms, the cluster appears remarkably isothermal at a given radius (see also Section 5.1). The average temperature, excluding the arms, rises from  $\sim 2$  keV at a radius  $r \sim 0.9$  arcmin ( $\sim 4$  kpc) to  $\sim 2.7$  keV by the edge of the field ( $r \sim 8.5$  arcmin). The X-ray

bright, cold arms appear to be the most significant departures from spherical symmetry. Surface brightness discontinuities at  $r \sim 3.75$  (northwest of the AGN) and  $r \sim 8$  arcmin (south of the AGN) noted by Forman *et al.* (2005) do not have clear, corresponding features in these maps.

The pressure map shown in Fig. 3 (Fig. 6b with 90 cm radio contours from Owen *et al.* 2000) appears significantly more regular than the temperature map. The exception is a ring of high pressure at a radius of  $r \sim 3$  arcmin that is approximately  $\sim 0.7$  arcmin thick. Forman *et al.* (2007) also see a feature at this radius in their analysis and argue that it is consistent with an AGN driven shock propagating through the ICM with a Mach number of  $M \sim 1.2$ .

At the location of the cool arms, the observed pressure is somewhat lower. This is, however, likely an artefact due to the strong, projected multi-temperature structure in the direction of the X-ray bright arms in these regions (Paper I).

The entropy map (Fig. 4) reveals a similar morphological structure to the temperature map. The cool, X-ray bright arms have significantly lower entropy than the ambient ICM at the same radius. This suggests that the gas within the arms originates from the low entropy central regions of the cluster. The detailed thermodynamics of the arms are discussed in Paper I.

The metallicity of the ambient cluster gas (Fig. 5) peaks at a value of  $\sim 1.5$  solar near the core and drops to  $\sim 0.3$  near the edge of the field,  $r \sim 8.5$  arcmin (40 kpc). The southern region is also more metal rich than the north and will be discussed further in Section 4.2.

At first glance, our maps suggest a reduced metallicity within the X-ray bright arms with respect to the ambient gas (the green contours of 1 keV emission; see Paper I). However, this apparent decrement is likely a bias due to the complex multi-temperature structure within the arms (*e.g.* Buote 2000; Simionescu *et al.* 2008; Werner *et al.* 2008 and references within). The metallicity structure of the X-ray bright arms will be discussed further in Paper III.

A high metallicity structure is observed at a radius of  $r \sim 4.5$  arcmin to the west of the central AGN. This ridge connects with the high metallicity extension to the northwest of the core at a radius of  $r \sim 3.3$  arcmin. However, this ridge is not continuous, with some regions of low abundance mixed within. As discussed in Section 5.3, this structure is likely due to the uplift of cool, metal-rich gas in the wake of buoyantly rising, radio-emitting plasma. High metallicity ridges are also observed in the Perseus Cluster, Ophiuchus Cluster, and Abell 2204 (see Sanders *et al.* 2005; Million *et al.* 2010; Sanders *et al.* 2009).

### 3.2 Thermodynamic properties of the inner regions

Temperature and pressure maps for the central  $2 \times 2$  arcmin<sup>2</sup> ( $9.4 \times 9.4$  kpc<sup>2</sup>) region of M87 are shown on an enlarged scale in Fig. 7. The 6 cm (5 GHz) radio contours of Hines *et al.* (1989) have been overlaid. Fig. 8 shows the 0.6 – 2.0 keV residual X-ray image (extracted from Fig. 1) for the same central  $2 \times 2$  arcmin<sup>2</sup> region. A number of prominent features in the images have been labelled with arrows. Each labelled cavity is detected at more than the  $10\sigma$  statistical

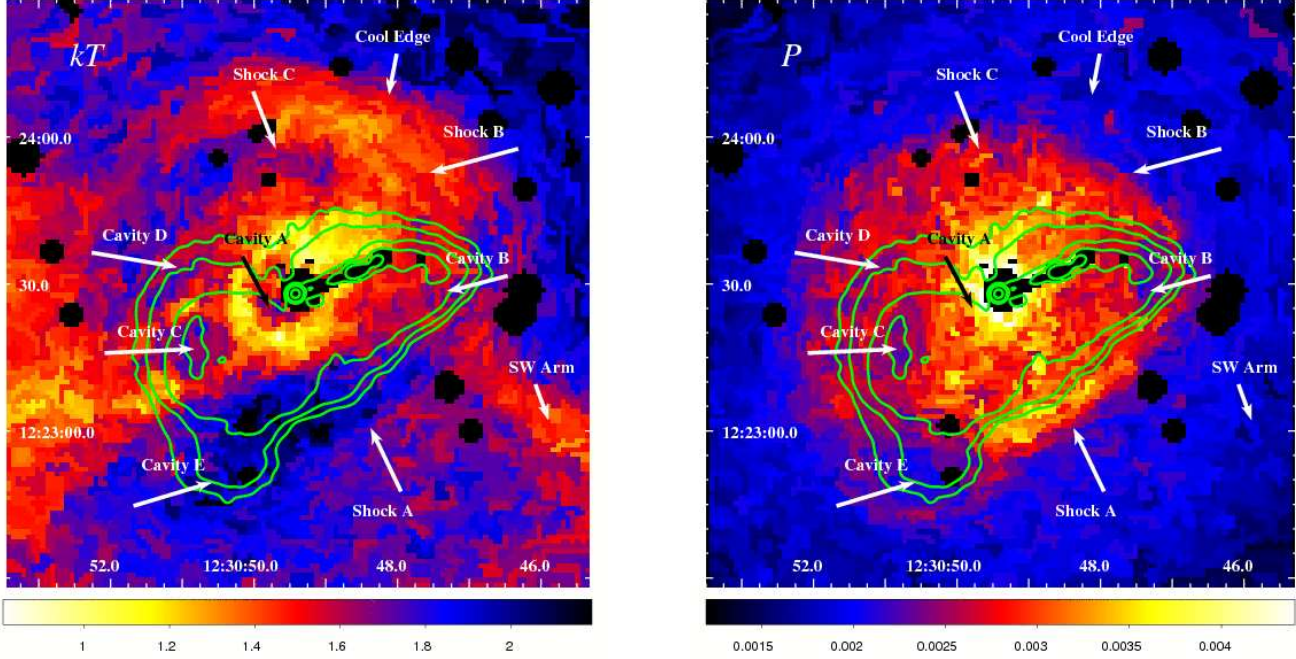


**Figure 7.** Thermodynamic maps (temperature on left; pressure on right) of the central  $2 \times 2$  arcmin<sup>2</sup> section of M87. Radio contours from Hines *et al.* (1989) are overlaid in green. Several notable features are labelled with arrows.

significance in surface brightness with respect to the smooth double- $\beta$  model.

The jets, which have a hard non-thermal spectral energy distribution (see *e.g.* Marshall *et al.* 2002; Wilson & Yang 2002; Perlman & Wilson 2005), would normally appear as bright, high pressure, hot structures in the maps, but have been masked in these images. At a radius of 7 arcsec (0.5 kpc) in the counter-jet direction, we observe a low X-ray surface brightness, hot cavity (‘A’) (see also Young *et al.* 2002). Interestingly, there is no obvious corresponding radio feature. A region of brighter, cooler gas encircles this structure and the AGN.

Several other low surface brightness cavities are visible in Fig. 8, in the jet and counter-jet directions (see also Forman *et al.* 2007). These correspond to regions of apparent low pressure and high temperature. Two of these cavities (labelled ‘B’ and ‘C’; both are at a radius of  $r \sim 40$  arcsec from the nucleus in the jet and counter-jet directions) are also filled with radio emitting plasma. Rings of cooler gas surround these cavities. The eastern-most cavity (‘D’), which also has relatively low pressure, lies at the edge of the radio cocoon that surrounds the AGN. Cavity E, labelled ‘bud’ by Forman *et al.* (2005), is located  $r \sim 40$  arcsec (3 kpc) to the south of the AGN and is associated with high temperature, low pressure gas and is filled with radio plasma. Surrounding the cavity is a rim of high pressure material that is possibly shocked gas.

The southwestern edge of the bright radio emission corresponds to a high pressure, high temperature, X-ray bright ‘ridge’. We identify this ridge as a shock front. This feature (labelled ‘Shock A’) may extend to surround most of the bright, inner radio cocoon; it is seen clearly to the northwest, though is less obvious to the east. The connecting ‘bridge’

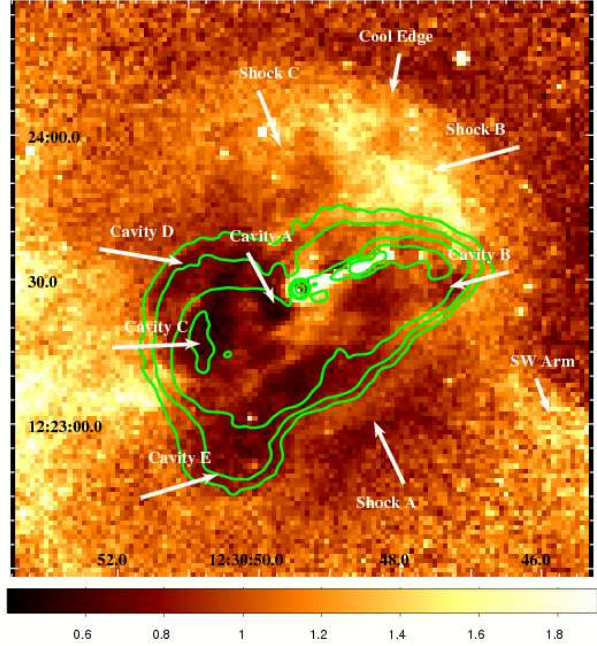


**Figure 8.** 0.6 – 2.0 keV surface brightness image divided by an azimuthally-symmetric double- $\beta$  model of the central  $2 \times 2$  arcmin<sup>2</sup> of Fig. 1. Other details as for Fig. 7.



between the central low temperature region and the southwest arm, which is also cool, appears ‘interrupted’ in projection by this shocked gas. To the northwest, for position angles of  $-63$ – $43$  degrees, at a radius of  $r \sim 40$  arcsec from the AGN, a coherent arc of relatively cool gas is observed. This cool gas is a multi-phase structure and is discussed in detail in Paper I. The outer edge of this arc at  $r \sim 50$  arcsec (labelled ‘Cool Edge’) is also probably physically linked to the central region of cooler gas, but is apparently broken up by the shock front (‘Shock B’ and ‘Shock C’).

## 4 AMBIENT GAS PROPERTIES

### 4.1 Azimuthally averaged projected profiles

Our thermodynamic mapping reveals, in exquisite detail, the complex structure of the bright X-ray arms (see also Paper I). Just as importantly, *Chandra*’s excellent spatial resolution also allows us to mask these structures and better determine the properties of the ambient gas surrounding M87. In this manner, we can avoid the complicating effects of temperature substructure, which will bias temperature and metallicity results in cases where the wrong thermal model is assumed (*e.g.* Buote 2000; Simionescu *et al.* 2008; Werner *et al.* 2008).

For this analysis, we use 36 annuli that vary in width from 10 to 30 arcsec, each with  $\sim 250,000$  net counts. Each region is fitted in the first case with a single temperature MEKAL spectral model, with Galactic absorption. We also repeat the analysis using the APEC code. The high signal-to-noise of our annular spectra allows us to constrain the abundances of O, Ne, Mg, Si, S, Ar, Ca, Fe, and Ni simultaneously, in addition to the temperature and normalization of the cluster gas (19 free parameters; 17 free parameters at large radius). Here we present results only for Fe. Results on elemental abundances other than Fe will be presented in a subsequent paper (Paper III). Error bars are drawn at the  $\Delta C = 1$  (68 per cent) confidence level.

Fig. 9 shows the projected profiles of the temperature and Fe abundance. Results are shown for both the APEC (filled circles) and MEKAL (open squares) plasma codes. Our profiles extend to the edge of the mosaic field of view,  $r \sim 8.5$  arcmin (40 kpc). The inner radius for these profiles is defined by the ‘Cool Edge’ identified at  $r \sim 50$  arcsec (4 kpc) in Fig. 7a.

The temperature profile (Fig. 9a) steadily rises from  $\sim 2.1$  keV to  $\sim 2.5$  keV for  $50 < r < 240$  arcsec. Beyond  $r \sim 4$  arcmin and out to  $r \sim 8.5$  arcmin, the temperature rises more slowly but again steadily, reaching  $kT \sim 2.7$  keV by  $r \sim 8.5$  arcmin. The statistical errors on the measured temperatures range from 0.3 to 0.8 per cent. The results for the two plasma codes exhibit slight differences, with the MEKAL temperatures being  $\sim 2$  per cent lower than those for APEC.

Careful inspection of Fig. 9a reveals a jump in temperature at a radius of  $r \sim 130$  arcsec. This corresponds to the inner edge of the shock front described in Section 3.1.

The Fe abundance profile (Fig. 9b) peaks at  $Z_{\text{Fe}} > 1.4$  solar in the central regions. The profile then exhibits a steady decline to  $Z_{\text{Fe}} \sim 0.7$  solar by  $r \sim 350$  arcsec. A significant enhancement, or ‘bump’, in the Fe abundance is

seen for radii  $350 < r < 400$  arcsec ( $27 - 31$  kpc). This is approximately the radius at which the bright X-ray arms terminate (see also Section 5.3).

We have investigated the impact of our choice of plasma code on the measured Fe abundances, finding a systematic offset of  $\sim 2$  per cent in the results for the MEKAL and APEC codes at lower temperatures. This offset rises to  $\sim 10$  per cent for the hottest gas observed at the edge of the field.

### 4.2 Southern and northern profiles

We have analyzed separately the properties of the ICM to the north and south of the X-ray bright arms.<sup>3</sup> Here, we have used the APEC plasma code only. Fig. 10 shows the projected temperature and Fe abundance profiles to the north (position angles  $-135$  to  $86$  degrees; filled circles) and south (position angles  $86$  to  $225$  degrees; open squares). Our results agree well with those of Simionescu *et al.* (2007) using *XMM-Newton* data.

The northern gas temperature profile is approximately constant at  $kT \sim 2.1$  keV for  $50 < r < 100$  arcsec, and then rises to  $\sim 2.7$  keV by 300 arcsec. Beyond this, the temperature rises only slightly out to  $r \sim 500$  arcsec. In contrast, the southern profile shows a stronger temperature gradient. The central 100 arcsec dips below 2 keV whilst at large radii  $r \sim 450$  arcsec the temperature rises to  $kT \sim 2.7$  keV.

The measured Fe abundance is consistently lower in the northern sector, presumably due to metal transport by sloshing (see Simionescu *et al.* 2010). For both the north and south, however, the Fe abundance peaks in the center and drops steadily out to a radius  $r \sim 400$  arcsec. To the north, we observe a bump of enhanced Fe abundance at  $330 < r < 400$  arcsec. A less significant bump is also observed to the south. This radius corresponds to the outer radius of the X-ray bright arms. A second large bump appears to begin at  $r \sim 500$  arcsec (39 kpc) to the north, which corresponds to the outer radius of the overall radio halo and suggests a similar origin. However, our profiles do not extend far enough to unambiguously confirm this feature. The southern profile shows no convincing evidence of Fe abundance enhancements at  $r \gtrsim 400$  arcsec.

## 5 DISCUSSION

### 5.1 Isothermality of the ambient cluster gas

The X-ray bright arms are well known to have multi-temperature structure (*e.g.* Belsole *et al.* 2001; Matsushita *et al.* 2002; Molendi 2002; Simionescu *et al.* 2008; Paper I). Previous spectral analyses have suggested that the gas outside of the X-ray bright arms is approximately isothermal at a given radius (Matsushita *et al.* 2002). Our data, however, allow us to study the spatial temperature structure in more detail. Such measurements have important implications for the physics of the ambient ICM, including *e.g.* the efficiency of thermal conduction and the assumption of hydrostatic equilibrium.

<sup>3</sup> The cool X-ray bright arms remain excluded in this analysis.

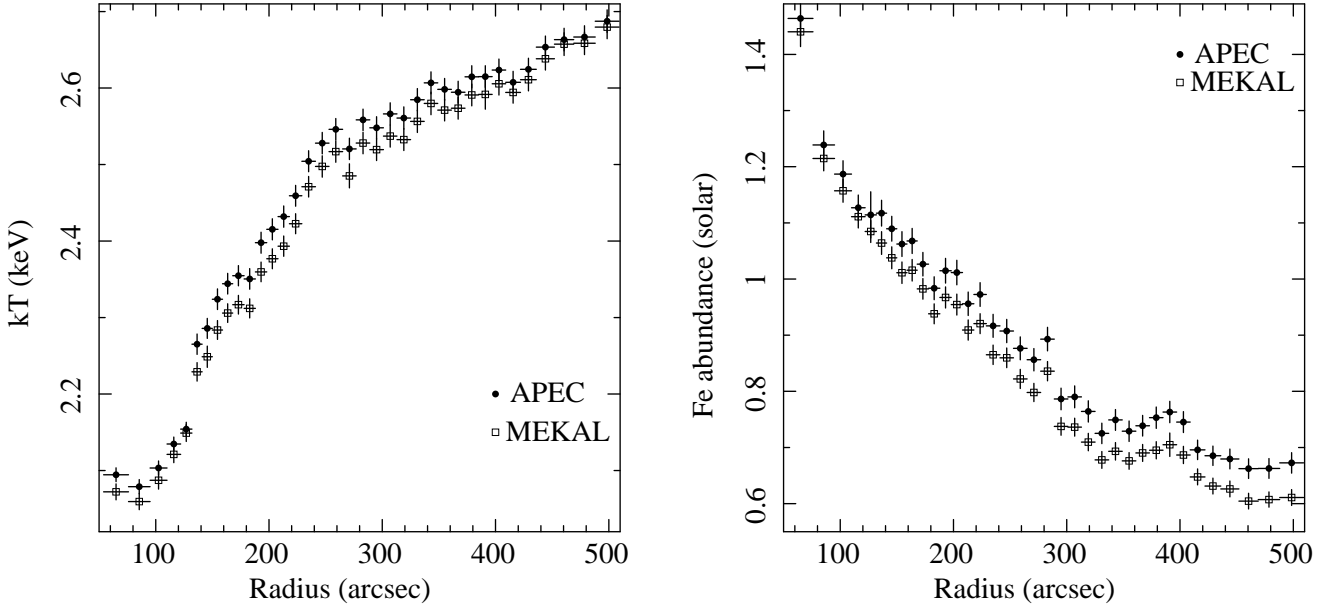


**Figure 9.** Azimuthally averaged, projected profiles of temperature (left; in keV) and Fe abundance (right) with respect to Lodders (2003) proto-solar abundances. Results are shown for both the MEKAL (open squares) and APEC (filled circles) plasma emission codes (Kaastra & Mewe 1993, Smith *et al.* 2001, respectively). A radius of 100 arcsec corresponds to a physical scale of 7.8 kpc. The X-ray bright arms are excluded from this analysis (see text). The fits for these spectra include the abundances of O, Ne, Mg, Si, S, Ar, Ca, Fe, and Ni as separate, free parameters in addition to the temperature and normalization of the cluster gas.

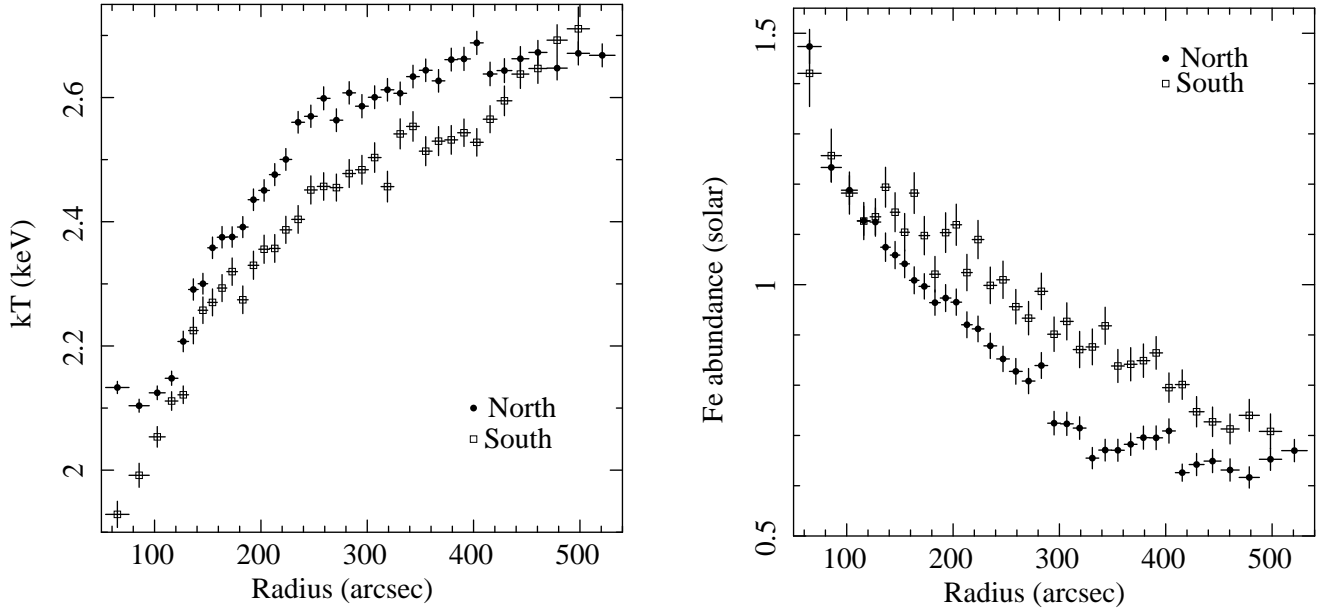


**Figure 10.** Projected profiles of the temperature (left; in keV) and Fe abundance (right; with respect to Lodders (2003) proto-solar abundances) for the northern and southern sectors, separately. Here we use the APEC plasma emission code only. Results for the northern sector (position angles -135 to 86 degrees) are plotted as filled circles. Results for the southern sector (position angles 86 to 225 degrees) are shown as open squares.

To determine the presence of multi-temperature structure at a given radius, we have made histograms of our different measurements of  $kT$  in 0.3 arcmin wide annular regions (Fig. 12). The analysis was performed in eight annuli in the radial range of  $90 < r < 235$  arcsec. For this analysis, we use position angles of -81–42 degrees. The width of the annuli was chosen to be large enough that  $\sim 75$  different bins from the thermodynamic maps are present in each. For this

analysis, we use the temperature map created with at least 2,500 net counts per region. The spectral models fitted to the individual spectra have the abundance ratios fixed to the best-fit values determined from the analysis described in Section 4.1 (see Section 5.1.1; see also Paper III).

We have also tested each individual region for spectral evidence of multi-temperature structure. A 4 temperature model (see Paper I) shows an absence of any significant ther-



mal emission at temperatures between  $0.5 < kT < 1.5$  keV at larger than the few per cent level (see also Fig. 11).

Having determined the distribution of temperature measurements, we compare this distribution with a Gaussian model. The width of the Gaussian is set to be equal to the average statistical error per bin (the typical standard deviations are approximately 3–5 per cent). Errors in each bin were determined from an MCMC analysis having chain lengths of at least  $10^4$  samples, after correcting for burn-in. A good match between the temperature measurements and the Gaussian model would be consistent with isothermality. Fig. 13 shows the ratio of the observed width of the emission measure distribution (labelled  $\sigma$ ) divided by the expectation, given the observed mean statistical error (labelled  $\delta$ ).

Only one out of 8 regions show evidence for a deviation from isothermality. This region is located at the temperature discontinuity behind the shock front. The temperature distribution in the other seven regions is consistent with being isothermal. Projection effects are not expected to have a significant influence on the analysis.

The observed isothermality at a given radius implies either that the ambient cluster gas beyond the arms is relatively undisturbed by AGN uplift, or that there is efficient conduction within a spherical shell. If conduction is responsible for the observed isothermality at a given radius, then the likely orientation of the magnetic fields is perpendicular to the radial direction, as expected under action of the heat-flux buoyancy instability (Quataert 2008; see also *e.g.* Bogdanović *et al.* 2009; Parrish *et al.* 2009).

Visual inspection of Fig. 5 also suggests that the metals in the ambient ICM are significantly clumped. A detailed analysis of the metal distribution and a discussion of the implications for turbulence and conduction in the ICM will be presented in future work.

### 5.1.1 Temperature bias

Fig. 14 shows the temperature (left) and metallicity (right) profiles measured from both the peaks of the emission measure distributions for the individual regions (open squares) and from the integrated annular spectra presented in Section 4 (filled circles). The temperature and metallicity results from the two techniques are systematically different by 10 and 30 per cent respectively. The magnitude of this offset decreases as a function of radius.

From spectral simulations, we have determined that this bias is a combined modelling and signal-to-noise issue. Low temperature spectra (below  $\sim 3$  keV) contain a strong line contribution at energies where *Chandra*'s effective area is the largest. However, in low signal-to-noise spectra, one cannot determine the abundances of individual elements separately. These are instead implicitly tied to the Fe abundance. The flux from line emission is, therefore, modelled improperly which biases the temperature and metallicity to low values. Increasing the signal-to-noise of the spectra reduces these biases, while simultaneously causing the residuals around the Fe L complex to significantly increase. The apparent position dependence is, therefore, explained by the temperature dependence of the intensity of these line components. The bias in low signal-to-noise spectra can be lessened by fitting a model with the abundance ratios of the individual ele-

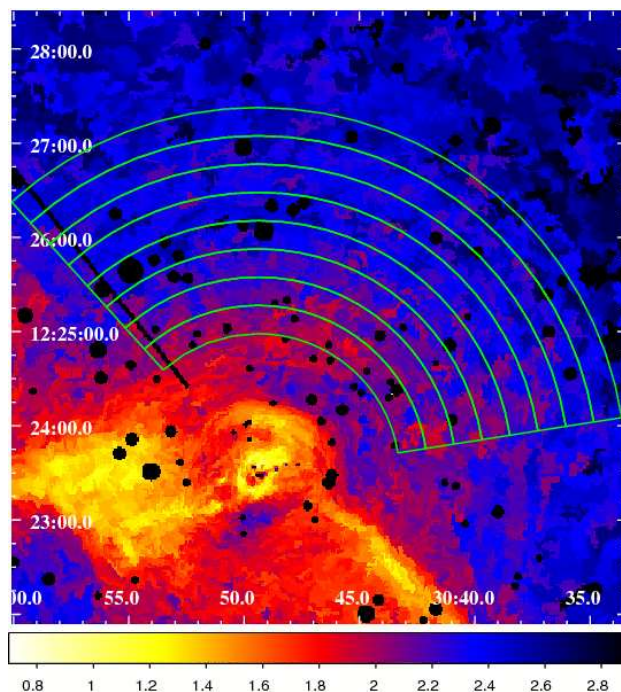


**Figure 11.**  $6.5 \times 6.5$  arcmin<sup>2</sup> section of the temperature map made with regions that contain  $\sim 2,500$  net counts. The 8 partial annuli used in the analysis are overplotted in green. The average error per bin  $\sim 5$  per cent in temperature.

**Table 2.** Summary of the shock models for each of the 4 different surface brightness profiles. Columns list the position angles of included data, shock radius, and Mach number of the observed shock within each position angle range. Conservative uncertainties on the Mach number, which bracket the observed scatter in the surface brightness profiles, are estimated to be  $M \pm 0.04$ .

Position Angle (degrees)	$r$ (arcsec)	$M$
20–50	182	1.16
190–220	168	1.29
320–350	188	1.21
350–20	180	1.34

ments adjusted to their best-fit values, as determined from a fit to the higher signal-to-noise spectra.

We emphasize that this bias does not affect the primary conclusions of this paper. Where appropriate, we have used the abundance ratios measured from the high signal-to-noise radial analysis (see Paper III) to reduce the impact of this effect.

## 5.2 Analysis of the shock fronts

### 5.2.1 The pressure ring at $r \sim 180$ arcsec (14 kpc)

The large-scale pressure map (Fig. 3) reveals the presence of a thick ( $\sim 40$  arcsec) high pressure ring at  $\sim 180$  arcsec. This feature has previously been identified as a shock with Mach number  $M \sim 1.2$  and age  $\sim 14$  Myrs (Forman *et al.* 2007).

Fig. 15 shows the projected surface brightness (upper

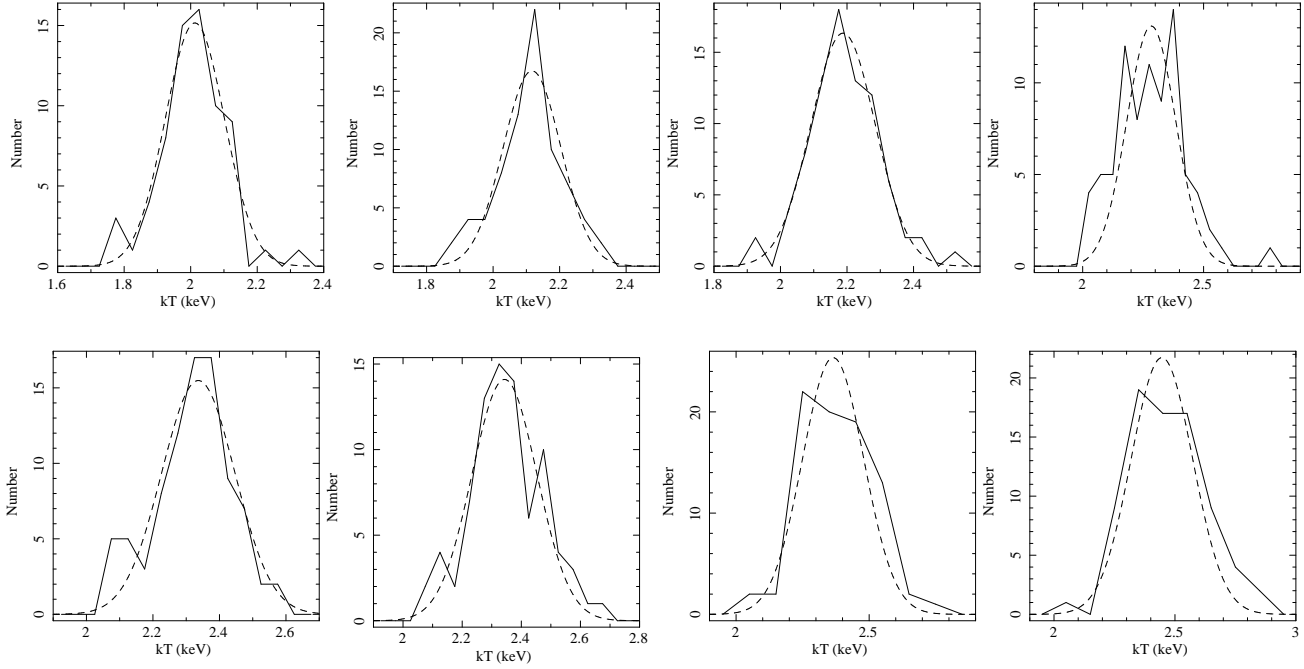


**Figure 12.** Histograms of temperature measurements (in keV) for all 8 regions. Each region contains  $\sim 75$  independent temperature measurements. Gaussians with standard deviation equal to that of the average measurement error per bin are overplotted (dashed lines). Only one region shows significant deviation away from isothermality.

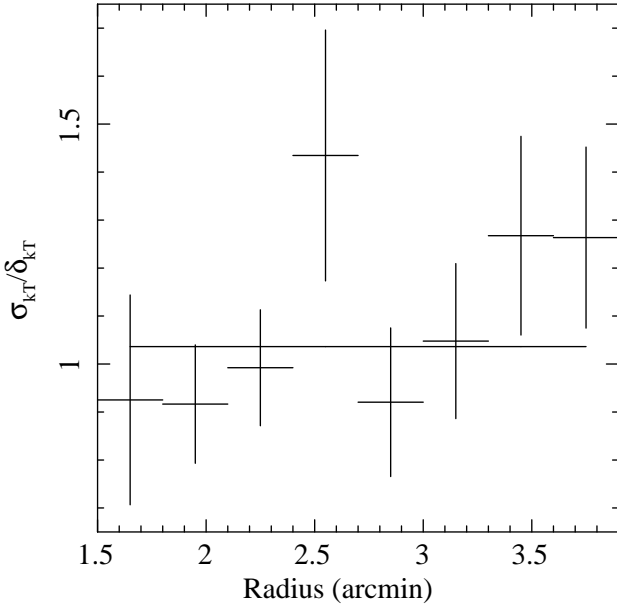


**Figure 13.** The ratio of the standard deviation of a Gaussian model fitted to the observed temperature distribution ( $\sigma$ ) and the average error per bin in the thermodynamic maps ( $\delta$ ) as discussed in Section 5.1. The ratio of errors is consistent with a constant value, which is overplotted on the data.

panels; in  $\text{cts s}^{-1} \text{ arcsec}^{-2}$ ) for the position angles 190–220 (south of the AGN; left) and position angles 350–20 (north of the AGN; right). These surface brightness profiles show signatures commensurate with a weak shock at a radius of  $r \sim 180$  arcsec. The relevant features occur at a slightly smaller radius to the south with respect to the north ( $r \sim 170$  as opposed to  $r \sim 180$  arcsec). Overplot-

ted on these profiles are simple shock models for a range of Mach numbers: for the northern sector, Mach numbers of 1.30, 1.34 and 1.38; for the southern sector, Mach numbers 1.24, 1.29 and 1.33.

The shock models assume a spherically symmetric, hydrodynamic model of a point explosion in an initially isothermal, hydrostatic atmosphere. The initial gas density profile is assumed to be a power law, which is adjusted to match the observed surface brightness profile beyond the shock (Nulsen *et al.* 2005a; Simionescu *et al.* 2009). We have also explored a model that injects a constant amount of energy per unit time into the system. This model provides no significant change to the calculated surface brightness profile, which is already fit well by the simple point explosion model.

These models show good overall agreement with the data and the analysis performed by Forman *et al.* (2007). Table 2 shows the Mach number and shock radius from 4 different 30 degree wedges (from  $-40$ – $50$  degrees and also from  $190$ – $220$  degrees). Systematic uncertainties dominate the modelling of the surface brightness in these wedges. These include any projected non-sphericity of the shock due to the likely jet axis alignment near our line of sight, and the incorrect assumption of an initially isothermal, hydrostatic atmosphere. We, therefore, do not include standard, statistical error bars from the models. Instead, we estimate the uncertainty in the Mach number by finding a Mach number which brackets the observed scatter in the surface brightness profiles (see Fig. 15). This represents a conservative estimate of the uncertainty in the Mach number of the shock. The overall shape of the surface brightness constrains the Mach number of the shock to within  $\sim 5$  per cent. The radius and Mach number of the shock vary at the ten per cent level as



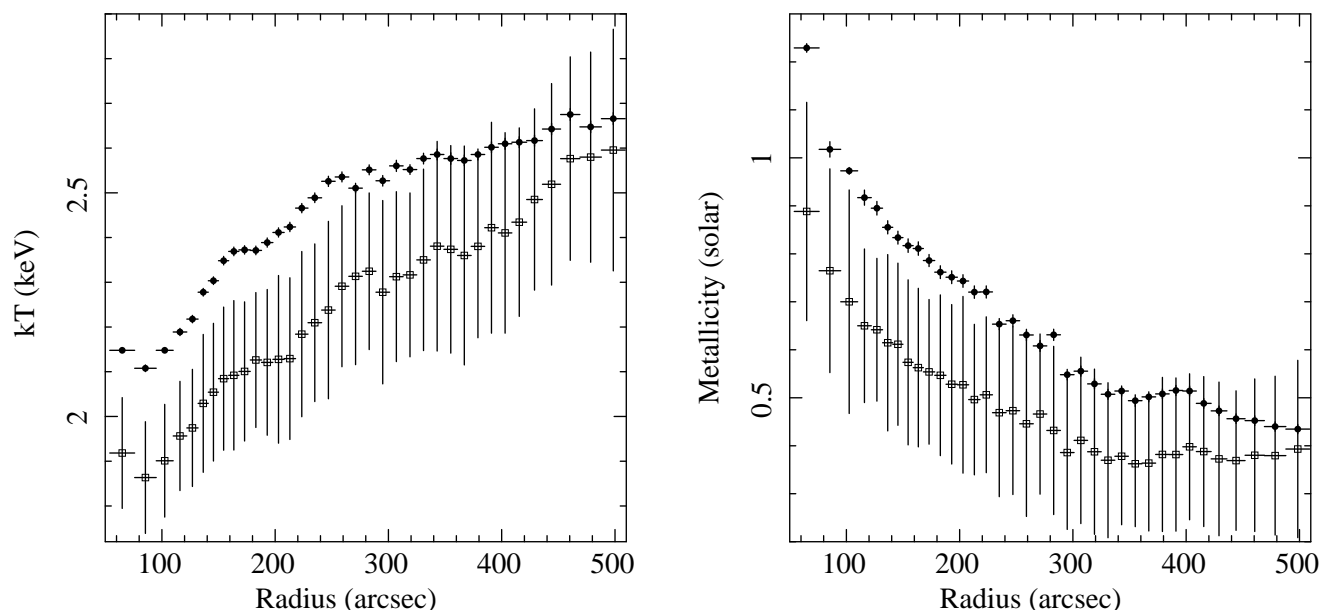


**Figure 14.** Temperature (left) and metallicity (right) measured from the mean of the emission measure distribution when fit with a Gaussian (open squares) and from the integrated spectrum using 250,000 net counts and the same, simple spectral model for the same annular regions in Section 4 (filled circles). The spectral model is a single phase temperature model with elemental abundances tied to Fe. Both the temperature and metallicity are systematically offset by 10 and 30 per cent respectively when measured with the two techniques. This is due to the incorrect modelling of the line emission around the Fe L complex, where *Chandra*’s effective area is largest.

function of position angle. This is likely due to the detailed structure of the ambient gas and shock front in each sector.

The temperature profiles for the position angles of  $-135 - 86$  and  $86 - 225$ , drawn from Fig. 10, are shown in the lower panels of Fig. 15. We have approximated the ambient temperature profile as a linear fit to the plotted data range, excluding the bins within the  $\sim 40$  arcsec thick shock. Under this assumption, we observe that both the northern and southern projected temperature profiles contain at least four bins (between  $130 \lesssim r \lesssim 170$  arcsec) that appear hotter ( $\sim 5$  per cent) than expected. Fig. 16 shows the expected projected temperature profile divided by the pre-shock temperature profile as a function of radius. The  $\sim 5$  per cent rise in the temperature and the  $\sim 40$  arcsec thick shock in the observed, projected temperature profile are fully consistent with the shock model given an average Mach number  $M = 1.25$  (see Fig. 16). We, therefore, conclude that the high pressure ring is consistent with a shock with  $M = 1.25$ .

Thick shocks have also been observed in the Perseus Cluster (see Fabian *et al.* 2006), which does not show a clear temperature jump at the leading edge of the front. The small increase in temperature within the thick over-pressurized ring in M87 suggests that shock heating is present in these systems but that the thickness and the small amount of heating associated with these weak shocks makes temperature increases difficult to detect.

### 5.2.2 The inner shock

A second shock is seen closer to the core ( $\sim 40$  arcsec; Section 3.2; Fig. 7). The properties of this shock are difficult to constrain due to its proximity to the core. Many other surface brightness features (*e.g.* the cavities filled with radio plasma seen in Fig. 7) are observed at similar radii, prevent-

ing an accurate determination of the pre-shock gas properties and the Mach number. However, the projected temperature jump seen to the south of the AGN at  $r \sim 40$  arcsec (3 kpc; Fig. 7), suggests a Mach number of at least  $M \gtrsim 1.2$ .

The presence of the two shocks suggests that AGN outbursts are fairly common. The estimated Mach numbers from these shocks and their relative distances can be used to determine the frequency of these outbursts. These shocks suggest that AGN outbursts occur approximately every  $\sim 10$  Myrs. Shock heating is likely only relevant in the central regions of the cluster because shocks significantly weaken as they expand. If repeated shocks occur every  $\sim 10$  Myrs, as is suggested here, then AGN driven, weak shocks could produce enough energy to offset the radiative cooling of the ICM (Nulsen *et al.* 2007).

### 5.3 Uplift of cool, metal-rich gas

Böhringer *et al.* (1995; see also Churazov *et al.* 2001) propose that rising bubbles filled with radio emitting plasma may be responsible for dragging cool, metal-rich gas up out of the central regions of clusters. Buoyant bubbles will rise to a height that depends on their entropy, stopping when they reach their appropriate adiabat. This process may explain the observed radio edges at  $r \sim 300 - 400$  arcsec (23–31 kpc) and also at  $r \sim 400 - 500$  arcsec (31–39 kpc). When the bubbles reach their maximum height, they flatten. A consequence of this interpretation is that metal-rich gas rising with the radio bubbles should be deposited at a radius similar to that at which the bubbles flatten. Our abundance profiles show evidence for enhancements in Fe abundance at  $320 < r < 400$  arcsec (see Figs. 9b, 10b). This is a similar radius to the outer edges of the X-ray arms. Indeed, bumps

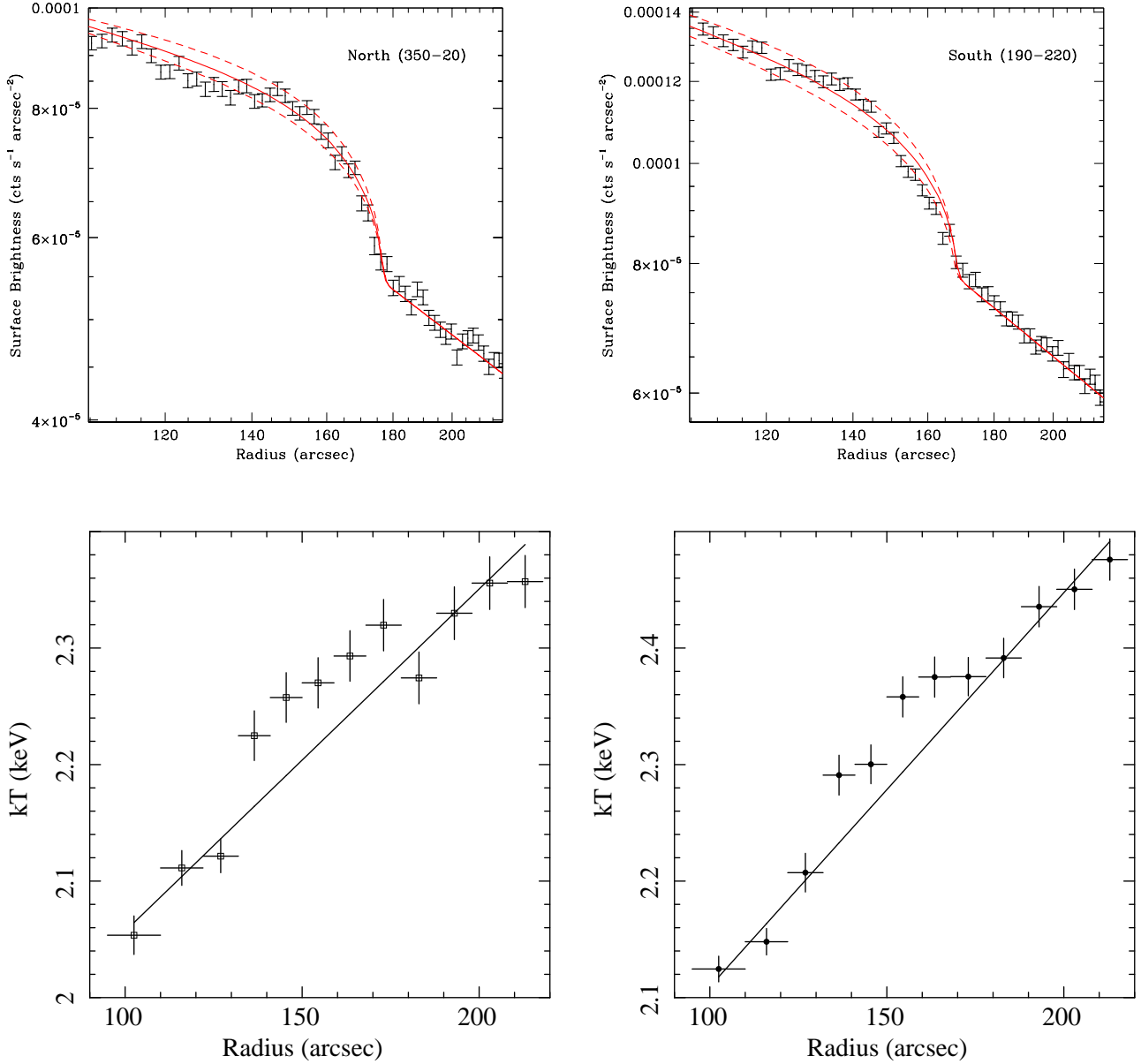


**Figure 15.** Projected surface brightness (top; in  $\text{cts s}^{-1} \text{arcsec}^{-2}$ ) for position angles 190–220 (left) and position angles 350–20 (right). The projected temperature profiles (bottom; in keV) are drawn from Fig. 10 (left is south; right is north). The surface brightness profiles show a clear discontinuity at  $\sim 170 - 180$  arcsec, corresponding to the outer edge of the shock. For the southern sector (position angles 190–220; left) shock models with Mach numbers 1.25, 1.29, and 1.33 at a radius of 168 arcsec are plotted; for the northern sector (position angles 350–20; right), models with Mach numbers 1.30, 1.34, and 1.38 at a radius of 180 arcsec are shown. The overplotted spread in Mach numbers represent a conservative estimate for the uncertainty in the measured Mach number. For the temperature profiles, we approximate the ambient temperature profile as linear fits to the temperature profiles in the plotted radial range, excluding temperature bins within the  $\sim 40$  arcsec thick shock. The projected temperature in the region of the shock is  $\sim 5$  per cent hotter than the best fit ambient model.

are observed in the abundance profiles of all elements except Oxygen (Paper III).

The amount of Fe that is uplifted can be determined from the excess metallicity measured at that radius and the gas mass. In detail,

$$M_{\text{Fe}} = M_{\text{g}} \times \Delta Z_{\text{Fe}} \times f_{\text{Fe}}, \quad (1)$$

where  $M_{\text{Fe}}$  and  $\Delta Z_{\text{Fe}}$  are the mass and excess abundance

of Fe,  $M_{\text{g}}$  is the gas mass, and  $f_{\text{Fe}} = \langle m_{\text{Fe}} \rangle / \langle m_{\text{i}\odot} \rangle \times (N_{\text{Fe}} / \sum_{\text{i}} N_{\text{i}})_{\text{odd}}$  is the mass fraction of Fe (Lodders 2003). We measure the gas mass and excess Fe abundance in the northern sector from a deprojection analysis (using data from position angles of  $-108$ – $55$  degrees). This implies a total mass of uplifted Fe of  $\sim 1.0 \times 10^6 M_{\odot}$ . We compare this to the Fe mass currently present in the arms (Simionescu *et al.* 2008). For a gas mass of  $5 \times 10^8 M_{\odot}$  and an Fe abundance of 2.2,

those authors measure an Fe mass of  $1.5 \times 10^6 M_\odot$  in the X-ray bright, cool arms. Thus, a single generation of uplifted metals from buoyant bubbles is, in principle, enough to explain the observed excess Fe mass at large radius. It is unknown how much of the uplifted metals will remain at large radius after the bubbles flatten. Lower significance bumps at higher radius that coincide with previous generations of radio bubbles may argue that this process occurs over multiple generations. It is likely that the magnetic field configuration and its evolution will also have an impact (*e.g.* Bogdanović *et al.* 2009). In the Perseus Cluster, metallicity enhancements also correspond well to the edges of several radio lobes, which suggests a similar origin to that discussed here (see Sanders *et al.* 2005). This process may also partly explain the metallicity ridges observed around the central regions of some cool core galaxy clusters (Sanders *et al.* 2005; Sanders *et al.* 2009; Million *et al.* 2010).

We note that bumps in the Fe abundance profiles are not clearly observed to the south. However, the mean Fe abundance is larger in the south than in the north and a cold front is located at a similar radius (Simionescu *et al.* 2007, 2010), making the identification of such a bump more difficult. Our results support the rising and pancaking bubble simulations presented in Churazov *et al.* (2001; see also *e.g.* Brüggen & Kaiser 2002; Kaiser 2003; Brüggen 2003; Ruzkowski *et al.* 2004a,b; Heinz & Churazov 2005).

## 6 SUMMARY

Utilizing a detailed, spatially-resolved spectral mapping and an ultra-deep (574 ks) *Chandra* observation of M87 and the central regions of the Virgo Cluster, we present an unprecedented, close-up view of AGN feedback in action. Our maps reveal X-ray bright arms that have been lifted up by buoyant radio bubbles as relatively cool, low entropy features that are rich in structure (see *e.g.* Belsole *et al.* 2001; Molendi 2002). The detailed properties of these arms are discussed in Paper I. Outside the arms, the ambient cluster gas is strikingly isothermal at each radius. This suggests that either the gas remains relatively undisturbed by AGN uplift or that conduction is efficient along the azimuthal direction, as expected under action of the heat-flux buoyancy instability (HBI). Many cavities are seen in the inner radio cocoon ( $\sim 40$  arcsec or  $\sim 3$  kpc) including one located at  $\sim 7$  arcsec ( $\sim 0.5$  kpc) from the central AGN in the counter-jet direction. These cavities are associated with decreased surface brightness, high temperatures, low thermal pressure, and typically appear filled with radio plasma in projection.

Our pressure map confirms spectrally previous results on the presence of a circular shock front at  $r \sim 180$  arcsec (14 kpc). Based on the surface brightness jump, we measure an average Mach number of  $M = 1.25$  for the shock at  $r \sim 180$  arcsec, in good agreement with the analysis of Forman *et al.* (2007). Under the assumption of a linearly rising temperature profile, we also measure a temperature jump within the  $\sim 40$  arcsec thick shock, consistent with the expectations for a shock with Mach number  $M = 1.25$ . The thickness and overall weakness of these shocks will make it difficult to detect temperature jumps unambiguously in hotter clusters like Perseus (*e.g.* Fabian *et al.* 2006; Graham *et al.* 2008).

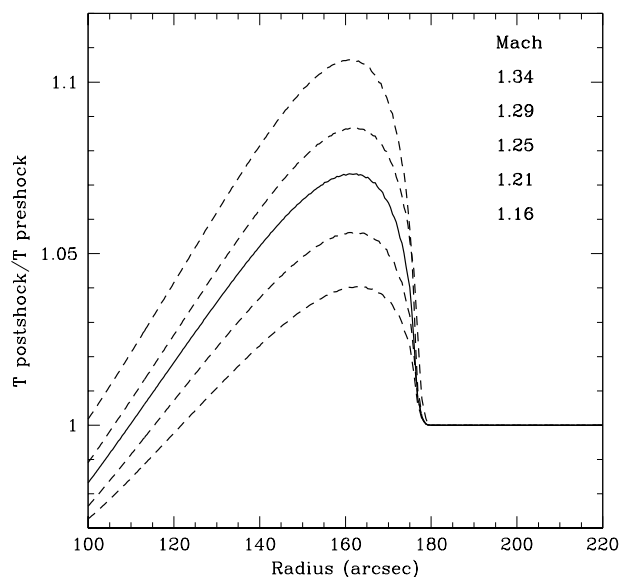


**Figure 16.** Expected emission weighted projected temperature profile divided by the pre-shock temperature given the Mach numbers determined from the shock models in 4 angular sectors. The average shock with Mach number  $M = 1.25$  at a radius of  $r = 180$  arcsec is represented by the solid line. The observed  $\sim 5$  per cent increase in temperature and the  $\sim 40$  arcsec thickness of the overpressurized region is well explained by the shock model.

Another shock, associated with the central radio cocoon, is observed at  $\sim 40$  arcsec ( $\sim 3$  kpc). Because of the complexity of this region, we can only estimate the Mach number of this shock, using the observed projected temperature jump across the front. This suggests a Mach number of  $M \gtrsim 1.2$ . The relative distances and Mach numbers of these shocks suggest that AGN outbursts are common and occur every  $\sim 10$  Myrs.

Our results show that a significant mass of metals is lifted up to large radius in the wake of the radio bubbles. At least  $1.0 \times 10^6 M_\odot$  of Fe is uplifted to a radius of 350 – 400 arcsec (27–31 kpc) to the north of the AGN. Given that a similar amount of Fe ( $1.5 \times 10^6 M_\odot$ ) is present in the X-ray bright arms (Simionescu *et al.* 2008), a single generation of bubbles can, in principle, explain the observed Fe excess. It is still uncertain how much metal falls towards the central regions after this process occurs. Fe uplift of this magnitude may explain the observed metallicity ridges observed around some cool core clusters. Studies of such abundance features can further enhance our understanding of transport processes. This will be the subject of future work.

## 7 ACKNOWLEDGMENTS

We thank W.R. Forman, C. Jones, and E. Churazov for helpful comments and R.G. Morris for computational support. N. Werner and A. Simionescu were supported by the National Aeronautics and Space Administration through Chandra/Einstein Postdoctoral Fellowship Award Number



PF8-90056 and PF9-00070 issued by the Chandra X-ray Observatory Center, which is operated by the Smithsonian Astrophysical Observatory for and on behalf of the National Aeronautics and Space Administration under contract NAS8-03060. This work was supported in part by the US Department of Energy under contract number DE-AC02-76SF00515. All computational analysis was carried out using the KIPAC XOC compute cluster at Stanford University and the Stanford Linear Accelerator Center (SLAC).

## REFERENCES

- Arnaud K.A., 1996, in *Astronomical Data Analysis Software and Systems V*, eds. Jacoby G. and Barnes J., ASP Conf. Series volume 101, p17
- Balucinska-Church M., McCammon D., 1992, *ApJ*, 400, 699
- Belsole E. *et al.* 2001, *A&A*, 365L, 188
- Bogdanović T., Reynolds C.S., Balbus S.A., Parrish I.J., 2009, *ApJ*, 704, 211
- Böhringer H., Nulsen P.E.J., Braun R., Fabian A.C., 1995, *MNRAS*, 274L, 67
- Böhringer H., Matsushita K., Churazov E., Ikebe Y., Chen Y., 2002, *A&A*, 382, 804
- Brüggen M. & Kaiser C.R., 2002, *Nature*, 418, 301
- Brüggen M., 2003, *ApJ*, 592, 839
- Buote D.A., 2000, *MNRAS*, 311, 176
- Churazov E., Brüggen M., Kaiser C.R., Böhringer H., Forman W., 2001, *ApJ*, 554, 261
- Croston J.H. *et al.* 2009, *MNRAS*, 395, 1999
- De Young D.S., 2003, *MNRAS*, 343, 719
- Fabian A.C., Sanders J.S., Allen S.W., Crawford C.S., Iwasawa K., Johnstone R.M., Schmidt R.W., Taylor G.B., 2003, *MNRAS*, 344L, 43
- Fabian A.C., Sanders J.S., Taylor G.B., Allen S.W., Crawford C.S., Johnstone R.M., Iwasawa K., 2006, *MNRAS*, 366, 417
- Feigelson E.D., Wood P.A.D., Schreier E.J., Harris D.E., Reid M.J., 1987, *ApJ*, 312, 101
- Forman W. *et al.* 2005, *ApJ*, 635, 894
- Forman W. *et al.* 2007, *ApJ*, 665, 1057
- Graham J., Fabian A.C., Sanders J.S., 2008, *MNRAS*, 391, 1749
- Gitti M., McNamara B.R., Nulsen P.E.J., Wise M.W., 2007, *ApJ*, 660, 1118
- Heinz S. & Churazov E., 2005, *ApJ*, 634L, 141
- Hines D.C., Eilek J.A., Owen F.N., 1989, *ApJ*, 347, 713
- Kaastra J.S., Mewe R., 1993, *Legacy*, 3, 16
- Kaiser C.R., 2003, *MNRAS*, 343, 1319
- Kalberla P.M., Burton W.B., Hartmann Dap, Arnal E.M., Bajaja E., Morras R., Poeppel W.G.L., 2005, *A&A*, 440, 775
- Kraft R.P., Vázquez S.E., Forman W.R., Jones C., Murray S.S., 2003, *ApJ*, 592, 129
- Lodders K., 2003, *ApJ*, 591, 1220
- Marshall H.L., Miller B.P., Davis D.S., Perlman E.S., Wise M., Canizares C.R. & Harris D.E., 2002, *ApJ*, 564, 683
- Matsushita K., Belsole E., Finoguenov A., Böhringer H., 2002, *A&A*, 386, 77
- McNamara B.R. & Nulsen P.E.J., 2007, *ARA&A*, 45, 117
- Million E.T., Allen S.W., Werner N., Taylor G.B., 2010, *MNRAS*, 405, 1624
- Molendi S., 2002, *ApJ*, 580, 815
- Nulsen P.E.J., McNamara B.R., Wise M.W., David L.P., 2005a, *ApJ*, 628, 629
- Nulsen P.E.J., Hambrick D.C., McNamara B.R., Rafferty D., Birzan L., Wise M.W., David L.P., 2005b, *ApJ*, 625L, 9
- Nulsen P.E.J., Jones C., Forman W.R., David L.P., McNamara B.R., Rafferty D.A., Birzan L., Wise M.W., 2007, in Böhringer H., Pratt G.W., Finoguenov A., Schuecker P., eds, *ESO Astrophys. Symp., Heating Versus Cooling in Galaxies and Clusters of Galaxies*. Springer-Verlag, Berlin, p. 210
- Owen F.N., Eilek J.A., Kassim N.E., 2000, *ApJ*, 543, 611
- Parrish I.J., Quataert E., Sharma P., 2009, *ApJ*, 703, 96
- Perlman E.S., Wilson A.S., 2005, *ApJ*, 627, 140
- Peterson J.R. & Fabian A.C., 2006, *PhR*, 427, 1
- Quataert E., 2008, *ApJ*, 673, 758
- Ruszkowski M., Brüggen M., Begelman M.C., 2004a, *ApJ*, 615, 675
- Ruszkowski M., Brüggen M., Begelman M.C., 2004b, *ApJ*, 611, 158
- Sakellou I. *et al.* 2002, *A&A*, 391, 903
- Sanders J.S., Fabian A.C., Dunn R.J.H., 2005, *MNRAS*, 360, 133
- Sanders J.S., 2006, *MNRAS*, 371, 829
- Sanders J.S., Fabian A.C., 2007, *MNRAS*, 381, 1381
- Sanders J.S., Fabian A.C., 2008, *MNRAS*, 390L, 93
- Sanders J.S., Fabian A.C., Taylor G.B., 2009, *MNRAS*, 393, 71
- Simionescu A., Böhringer H., Brüggen M., Finoguenov A., 2007, *A&A*, 465, 749
- Simionescu A., Werner N., Finoguenov A., Böhringer H., Brüggen M., 2008, *A&A*, 482, 97
- Simionescu A., Roediger E., Nulsen P.E.J., Brüggen M., Forman W.R., Böhringer H., Werner N., Finoguenov A., 2009, *A&A*, 495, 721
- Simionescu A., Werner N., Forman W.R., Miller E.D., Takei Y., Böhringer H., Churazov E., Nulsen P.E.J., 2010, *MNRAS*, 405, 91
- Smith R.K., Brickhouse N.S., Liedahl D.A., Raymond J.C., 2001, *ApJ*, 556L, 91
- Tonry J.L., Dressler A., Blakeslee J.P., Ajhar E.A., Fletcher A.B., Luppino G.A., Metzger M.R. Moore C.B., 2001, *ApJ*, 546, 681
- Werner N., Böhringer H., Kaastra J.S., de Plaa J., Simionescu A., Vink J., 2006, *A&A*, 459, 353
- Werner N., Durret F., Ohashi T., Schinder S., Wiersma R.P.C., 2008, *SSRv*, 134, 337
- Werner N. *et al.* , 2010, *MNRAS*, in press, astro-ph/1003.5334
- Wilson A.S., & Yang Y., 2002, *ApJ*, 568, 133
- Young A.J., Wilson A.S., Mundell C.G., 2002, *ApJ*, 579, 560